

Hierarchical Superhydrophobic Aluminum Surfaces for Condensation Applications

by

Ken Lopez

Submitted to the
Department of Mechanical Engineering
in Partial Fulfillment of the Requirements for the Degree of

Bachelor of Science in Mechanical Engineering

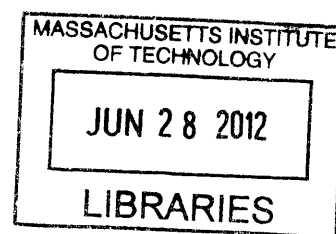
at the

Massachusetts Institute of Technology

May 2012

[June 2012]

ARCHIVES



©2012 Massachusetts Institute of Technology. All rights reserved.

Signature of Author
Department of Mechanical Engineering
May 25, 2012

Certified by
Associate Professor of Mechanical Engineering
Evelyn N. Wang
Thesis Supervisor

Accepted by
Samuel C. Collins Professor of Mechanical Engineering
John H. Lienhard V
Undergraduate Officer

Hierarchical Superhydrophobic Aluminum Surfaces for Condensation Applications

by

Ken Lopez

Submitted to the Department of Mechanical Engineering
on May 25, 2012, in Partial Fulfillment of the
Requirements for the Degree of
Bachelor of Science in Mechanical Engineering

Abstract

Many existing industrial systems, including thermal desalination plants and air conditioning systems, involve the process of condensation and are heavily dependent on this process for achieving adequate levels of energy efficiency. In order to obtain these levels of efficiency, condensation heat transfer must be optimized through the application of dropwise condensation. One ongoing solution for improving the performance of dropwise condensation is the implementation of superhydrophobic structures and chemistries on condensing surfaces. Aluminum, being a heavily utilized material in many condensing systems and other industrial applications, is the subject of the present study. This thesis presents methods for synthesizing aluminum surfaces to produce microstructured morphologies through chemical etching with hydrogen chloride and oxidation with sodium hydroxide. After functionalization of these surfaces with a hydrophobic surface coating, the surfaces were tested for condensation using optical microscopy and a high quality environmental chamber. From experimentation, condensed droplets on these surfaces were unable to achieve the proper Wenzel to Cassie-Baxter transition and produce a jumping behavior which is a necessary criterion for superhydrophobic condensation. However, the HCl etched aluminum surface was able to achieve heat transfer rates greater than the smooth, filmwise aluminum surface by a factor of 2 and greater than the smooth, dropwise aluminum surface by a factor of 5/3. This implies that these structures were still capable of improving heat transfer rates despite their inability to surpass the energy barrier required for superhydrophobic condensation.

Thesis Supervisor: Evelyn N. Wang

Title: Associate Professor of Mechanical Engineering

Acknowledgements

The accomplishments that I have made thus far in my life have not been achieved merely due to the struggle of a single individual but the efforts of many. Of these people include my family, whose ability to overcome unimaginable struggles in life have inspired me to become a person of ambition, desire, and passion. My sincere efforts in achieving my goals have been dedicated to my parents, who have long faced unthinkable challenges throughout their lives in order to give my sister and I what we have today. Success of this magnitude was never seen possible to my parents, who lived in extreme poverty and faced the many struggles as immigrants in this country, but I am here as a testimony to all that it is possible to reach such heights.

I also want to acknowledge my sister who has been my best friend and has always been there to make sure my head is screwed on straight. May she continue striving for her goals in school at Cornell and beyond. I would also like to acknowledge all my friends here at MIT because it is with my friends that I have been able to surpass the tough challenges and enjoy the simple pleasures of life with even just a couple of jokes. I have learned that without friends there is a lack of happiness and without happiness there is a lack of purpose, so it's the smiles on my friend's faces that keeps me going on.

I want to thank Dr. Ryan Enright for his years of guidance as my primary research mentor from the very beginning when I first joined the research group. He taught me everything I know in order to write this thesis and understand everything there is to know about the realms of the Wenzel and Cassie states. I want to thank him for teaching me to appreciate all aspects of research, from the observable to the non-tangible. I also want to acknowledge Nenad, whose charisma, personality, and simple way of being made me happy to get out of bed and head into lab despite how much I cherished my sleep. He has not only been a great research mentor but a source for advice in my life whenever I had troubling doubts about things inside and outside of the lab. Without Nenad I wouldn't have been able to finish this project, so I thank him for all his help. It's researchers like these that have motivated and inspired me to pursue higher levels of education. I'd also like to acknowledge all the students in the Device Research Laboratory that have played a role in my success in this project and for simply saying hello from time to time. Lastly, I would like to thank Professor Evelyn Wang for giving me this opportunity to work for her group and for her guidance upon making some critical decisions in my life, such as choosing to go to Stanford which I am really happy I did.

At the end of it all, I want this to be not only a thesis, but a statement to the world that "all is possible".

Contents

1	Introduction	13
1.1	Modes of Condensation	14
1.1.1	Filmwise Condensation	14
1.1.2	Dropwise Condensation	15
1.2	Superhydrophobicity: Surface Characterization for Dropwise Condensation	16
1.3	Non-condensable Gases	18
2	Experimental Models	20
2.1	Filmwise Condensation on Complex Geometry	20
2.2	Experimental Heat Transfer Model	22
3	Experimental Setup, Configuration and Procedures	24
3.1	Optical Microscopy Condensation Setup	24
3.2	Environmental Chamber and Sample Setup	25
3.3	Optical Microscopy Experimental Procedures	30
3.4	Environmental Chamber Experimental Procedures	31
4	Aluminum Sample Synthesis, Preparation and Characterization	33
4.1	Sample Synthesis and Preparation Procedures	33
4.2	Sample Characterization	35
5	Experimental Results and Discussion	41
5.1	Optical Microscopy Condensation Analysis	41
5.2	Environmental Chamber Condensation Results	42
6	Conclusions and Future Directions	47

List of Figures

1.1	Vertical wall film condensation. (a) mass balance and (b) energy balance along film [10].	14
1.2	Dropwise condensation on a vertical wall. Note that as the drops grow and coalesce they are pulled down by the force of gravity and wipe away other droplets in their path, creating new nucleation sites [10].	16
1.3	Wenzel and Cassie-Baxter droplet morphologies	17
2.1	Cross-sectional view of condensation along a circular tube [9].	21
2.2	Condensing vapor along outer tube with water at inlet and outlet. Temperature profile along the tube increases exponentially [10].	23
3.1	Schematic of setup used for initial condensation experiments.	25
3.2	Schematic of environmental chamber setup.	27
3.3	Front view configuration of environmental chamber.	28
3.4	Back view configuration of environmental chamber.	29
3.5	Sample setup for condensation experiments.	30
4.1	FESEM images of aluminum HCl 12 min etch at (a) 9600, (b)28320, (c)46160, (d)61120 magnifications.	36
4.2	FESEM images of aluminum HCl 16 min etch at (a) 15470, (b)26300, (c)94470, (d)56760 magnifications.	37
4.3	FESEM images of aluminum NaOH 15 min oxidation time at (a) 16250, (b)35810, (c)134100, (d)286450 magnifications.	38
4.4	FESEM images of aluminum hybrid sample of 4 min HCl etch and 20 min NaOH oxidation at (a) 21290, (b)31200, (c)78100, (d)298620 magnifications.	39

4.5	Equilibrium contact angle measurement images. (a) HCl 16 min etch, (b) NaOH 15 min oxidation time, (c) hybrid surface 4 min HCl etch, 20 min NaOH oxidation. . .	40
5.1	Condensation under optical microscopy. (a) onset nucleation HCl 12 min etch, (b) ~ 18 min time-lapse nucleation HCl 12 min etch, (c) onset nucleation NaOH 15 min oxidation time, (d) ~ 18 min time-lapsed nucleation NaOH 15 min oxidation time, (e) onset nucleation hybrid surface 4 min HCl etch, 20 min NaOH oxidation, (f) ~ 18 min time-lapse nucleation hybrid surface 4 min HCl etch, 20 min NaOH oxidation .	43
5.2	Condensation heat transfer results. The heat flux is plotted versus the superheat $T_{sat} - T_{wall}$. (a) results for the smooth, filmwise aluminum surface compared to Nusselt filmwise theory, (b) results for smooth, dropwise aluminum surface, and (c) results for the HCl etched superhydrophobic dropwise aluminum surface.	45
A.1	High levels of silane deposited onto aluminum surfaces. (a) HCl 12 min etch at 31.7kx, (b) HCl 12 min etch at 5.95kx, (c) HCl 16 min etch at 860x, (d) HCl 16 min etch 18.47kx, (e) NaOH 15 min oxidation 32.61kx, (f) hybrid 4 min HCl etch, 20 min NaOH oxidation at 124.69kx magnifications.	50

List of Tables

4.1 Measured Contact angles for three aluminum samples. 40

Chapter 1

Introduction

Condensation is a heat and mass transfer process that is classified under natural convection as it is driven by body forces exerted directly within the fluid as a result of cooling. This phenomena involves a change of phase, from vapor to liquid, and the release of latent heat of vaporization. This heat transfer mode is applied in many systems that we see today including multi-stage flash desalination systems, distillation in power plants and refineries, and even in air conditioning systems.

There are two idealized models for condensation: filmwise condensation and dropwise condensation. During filmwise condensation, vapor condenses onto the cold surface in droplets which grow by further condensation and coalesce to form a film; this occurs if the surface is wettable or hydrophilic. In dropwise condensation, the condensed droplets flow away and off the surface allowing new droplets to form; this takes place on non-wetting or hydrophobic surfaces. Dropwise condensation results in local heat transfer coefficients which are often an order of magnitude greater than those for filmwise condensation. Consequently, much focus has been put on developing non-wetting surfaces that can produce dropwise condensation.

Many surfaces have already been explored to exhibit hydrophobic characteristics which have potential for use in condensation applications. Superhydrophobic surfaces have yielded promising results for improving condensation heat transfer rates because they demonstrate large contact angles and low contact angle hysteresis. The characteristics of these surfaces are their micro- or nano-scale structures, which result in high roughness, and their hydrophobic surfaces chemistry.

The present goal is to explore surface engineering on aluminum surfaces for the application of condensation. Aluminum is an important subject of study because of its abundance in nature, ease of handling and it represents an important category of material due to its high technological value and its wide range of industrial applications [11]. The objective is to develop an easy and fast

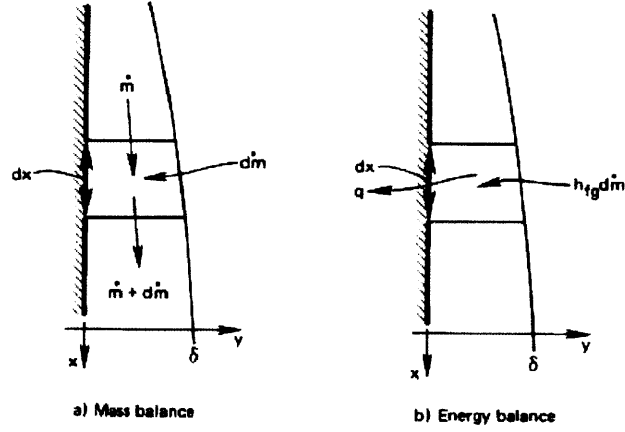


Figure 1.1: Vertical wall film condensation. (a) mass balance and (b) energy balance along film [10].

superhydrophobic surface fabrication process that can be implemented on commercially available condensation systems with aluminum. In this study two primary synthesis methods were explored: a chemical etch and an oxidation process. The detailed fabrication processes will be discussed in the latter as well as their effects on condensation heat transfer.

1.1 Modes of Condensation

1.1.1 Filmwise Condensation

Common surfaces have a characteristic of being wettable or hydrophilic, hence they can exhibit filmwise condensation in the presence of a higher temperature vapor. Due to the fact that latent heat of liquid is typically a very large number, a high heat transfer rate can result from very thin films. Filmwise condensation can be explained through a laminar film on a vertical plate as shown in Figure 1.1 with basic fundamental principles. The film condensate beings at the top and flows downward under gravity, resulting in a film with increasing thickness downward. The temperature profile across the film is linear and heat transfer is one-dimensional heat conduction across the film.

The approach used to develop a model for heat transfer in this film is an integral analysis method. By taking a small differential volume of the film, a force and energy balance is done in order to develop a relationship for the film thickness as a function of wall length, x [10].

$$\delta(x) = \left[\frac{4\mu_L k_L (T_{sat} - T_w) x}{\rho_L (\rho_L - \rho_G) g h_{L,G}} \right]^{1/4} \quad (1.1)$$

where the liquid properties are represented by a subscript L and the vapor properties by subscript G ; $h_{L,G}$ represents the latent heat of vaporization. Using the definition of the heat transfer coefficient and the Nusselt number, a local Nusselt correlation can be derived.

$$h = \frac{q}{T_{sat} - T_w} = \frac{1}{T_{sat} - T_w} \left[\frac{k(T_{sat} - T_w)}{\delta} \right] = \frac{k}{\delta} \quad (1.2)$$

$$Nu_x = \frac{hx}{k} = \frac{x}{\delta} \quad (1.3)$$

$$Nu_x = 0.707 \left[\frac{\rho_L(\rho_L - \rho_G)gh'_{L,G}x^3}{\mu_L k_L(T_{sat} - T_w)} \right]^{1/4} \quad (1.4)$$

To obtain an average Nusselt correlation, averaged about the length of the vertical wall, the local Nusselt function, Equation 1.4, is integrated along L , the length of the wall.

$$\overline{Nu_L} = 0.9428 \left[\frac{\rho_L(\rho_L - \rho_G)gh'_{L,G}L^3}{\mu_L k_L(T_{sat} - T_w)} \right]^{1/4} \quad (1.5)$$

This Nusselt model can now be used to predict the heat transfer coefficient in a condensing film, thus used to calculate the heat transfer rate using an energy balance.

1.1.2 Dropwise Condensation

Dropwise condensation may occur when condensation takes place on a surface that is not wetted by the condensate. During this process, vapor condenses onto the cold surface causing the onset of droplet growth. These droplets begin to merge and coalesce with neighboring droplets until the droplets are large enough to be pulled down by gravity. As the droplets accelerate downward on the wall surface, they collect other drops on their path and remove them from the wall leaving a dry swathe in its wake as shown in Figure 1.2. New nucleation sites are formed in these dry regions leading to the growth of more droplets. This continuous cycle of droplet removal and growth creates an efficient heat removal mechanism that leads to heat transfer coefficients as high as $200,000 \text{ W/m}^2 \text{ K}$ [10].

One of the major goals in dropwise condensation is to create surfaces that can sustain dropwise condensation for extended periods of time, thus avoiding hysteresis. Such surfaces that can accomplish such task are superhydrophobic surfaces, which will be discussed in the next section. The transition from dropwise to filmwise condensation is an issue in dropwise condensation and one that is not fully understood. Based on previously documented experiments, this transition has been

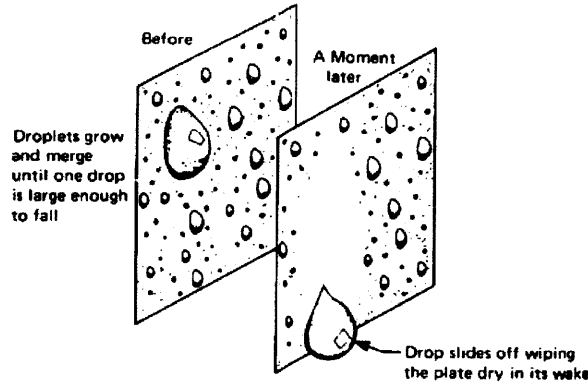


Figure 1.2: Dropwise condensation on a vertical wall. Note that as the drops grow and coalesce they are pulled down by the force of gravity and wipe away other droplets in their path, creating new nucleation sites [10].

associated with the increased proximity of active nucleation sites with increasing vapor-surface temperature difference and with the speed at which small or primary drops coalesce as compared with their growth rate [5].

Up to date, there has been no definitive model for explaining dropwise condensation other than empirical derivations. Therefore, this research area holds much room for improvements and advancements in understanding the mechanism involved in dropwise condensation. Furthermore, there has yet to be a practical implementation of a means of promoting dropwise condensation on industrial systems successfully. The present study aims to develop solutions for practical applications and to contribute to the understanding of the dropwise condensation phenomena.

1.2 Superhydrophobicity: Surface Characterization for Dropwise Condensation

Thermal processes that are dependent on condensation are a prime target for implementing superhydrophobic surfaces in order to improve efficiency. Traditionally, superhydrophobic surfaces are made by combining two steps that involve the creation of a rough micropattern in the first step and the passivation of the rough surface using a low surface energy coating the second step [7]. In order to exhibit superhydrophobic condensation, the surfaces under study must satisfy two principle criteria [4]. The first criterion involves a scale-invariant wetting energy which determines whether the contact line, between the droplet and the surface, remains pinned at the base of the droplet, leading to the Cassie-Baxter state, or if the contact line de-pins to form a Wenzel droplet; the criterion can be seen

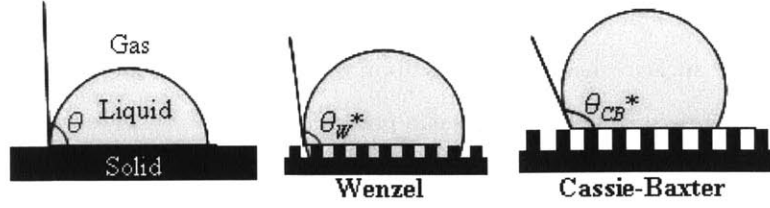


Figure 1.3: Wenzel and Cassie-Baxter droplet morphologies

in Figure 1.3 .

Using the non-equilibrium Wenzel equation [4]:

$$\cos\theta_a^W = r\cos\theta_a \quad (1.6)$$

where r is the surface roughness and θ_a is the advancing contact angle associated with the wettability of the given surface we can determine the pinning energy barrier during droplet growth. This characteristic energy barrier is compared to the reference equilibrium state through the Cassie-Baxter equation [4]:

$$\cos\theta^{CB} = \varphi(\cos\theta_e + 1) - 1 \quad (1.7)$$

where θ_e is the equilibrium contact angle. With the two given characteristics, a relationship that predicts the wetting state of the droplet morphology is developed:

$$E^* = \frac{\cos\theta^{CB}}{\cos\theta_a^W} = \frac{\varphi(\cos\theta_e + 1) - 1}{r\cos\theta_a} \quad (1.8)$$

If $E^* < 1$, the droplets will pin to the structures on the surface and spread over the top of the structures forming a Cassie-Baxter droplet. If $E^* > 1$, the droplet will penetrate the structures of the surface and de-pin forming a Wenzel droplet.

The second criterion for superhydrophobic condensation involves a scale requirement that links a characteristic size of roughness which defines the pinning energy barrier to the mean separation distance between nucleation sites. This criterion is not fully explored in the present study, however it is still an essential criterion to keep in mind for scalability purposes.

The primary goal for dropwise condensation is to successfully remove condensate from the condensed surface as quickly as possible before large drops form and add to thermal resistance of the liquid condensate. Typically, gravity is the mechanism of droplet removal, however, a recent study demonstrated the removal of condensate drops on a superhydrophobic surface without any external

forces [1]. Researches were able to achieve a spontaneous jumping motion of droplets out-of-plane that is powered by the surface energy released upon drop coalescence in-plane. By satisfying the two criterion above, superhydrophobic surface can potentially achieve this jump-like behavior during condensation and result in effective dropwise condensation [3].

1.3 Non-condensable Gases

One of the most significant issues in condensation processes is the presence of non-condensable gases which is a very prominent factor in most practical situations. When vapor that is condensing is mixed with non-condensable air, uncondensed air must diffuse away from the condensing film constantly and vapor must diffuse inward toward the film. Essentially, there are two coupled processes occurring simultaneously which significantly slows down the condensation rate; heat transfer rates have been shown to be reduced by fifty percent or more due to small amounts of non-condensable air present in a system.

The effect of non-condensables was first studied by Sparrow and Lin who devised a theory for predicting condensation in the presence of non-condensables [8]. They concluded that the presence of a very small amount of non-condensable gas in the bulk of the condensing vapor can cause a large buildup of noncondensables at the liquid-vapor interface. With increasing values of $c_{pL}(T_i - T_w)/\lambda Pr_L$, the mass fraction of non-condensables increases. This buildup at the interface causes the partial pressure of the condensing vapor at the interface to be reduced. Consequently, there is a reduction of the interface temperature T_i and a corresponding decrease in the heat transfer since the thermal driving force $(T_i - T_w)$ is decreased.

Non-condensable gas is transported from the bulk of the condensing vapor to the liquid-vapor interface by the same convective flow that is carrying the vapor which is to be condensed. The interface is impermeable to the non-condensables, hence non-condensables must be removed from the interface at the same rate at which it arrives in order to preserve steady-state conditions. The only way that this can happen is through diffusive flow from the interface back to the bulk of the vapor. Therefore, the concentration of non-condensables at the interface must reach a high enough value in order for the diffusive flow to occur from the higher concentration, at the interface, to the lower concentration, at the bulk vapor.

The ideal way to avoid the presence of non-condensables is to perform condensation experiments in a completely non-condensable environment or by entirely removing non-condensables from the experimental environment. In the present study, a high quality environmental chamber was used

to decrease the concentration of non-condensable present in the experiments. With this chamber, accurate data was taken and analyzed which yielded results of higher quality compared to an ambient non-condensable environment.

Chapter 2

Experimental Models

Much of the prior work on condensation with hydrophobic surfaces has been done on flat square samples with small areas. In order to understand condensation enhancements through the use of hydrophobic surfaces in a more realistic setting, the present condensation work was done using a complex geometry, aluminum tubes. There are some clear advantages in exploring condensation on this geometry:

1. the geometry is more representative of industrial applications; for example, heat exchangers with tube bundles
2. the length of the condensing section is longer hence increasing the signal to noise ratio due to the larger temperature gradient and larger surface area

The following will explore smooth aluminum tube surfaces with hydrophilic wetting characteristics, used as a baseline for comparison with the hydrophobic non-wetting surfaces. The synthesized aluminum tube surfaces with micro- and nano-scale roughness characteristics and hydrophobic surface chemistry are the primary focus of this study and will be covered extensively in the following. In order to understand the heat transfer enhancement of these structured, hydrophobic aluminum surfaces, the following will present the models used for validation and comparison.

2.1 Filmwise Condensation on Complex Geometry

In the present study, Nusselt theory for condensation on horizontal tubes will be applied in the validation of the experimental results conducted in the environmental chamber and for the comparison with the experimental dropwise condensation results. Just as the vertical plate derivation using the

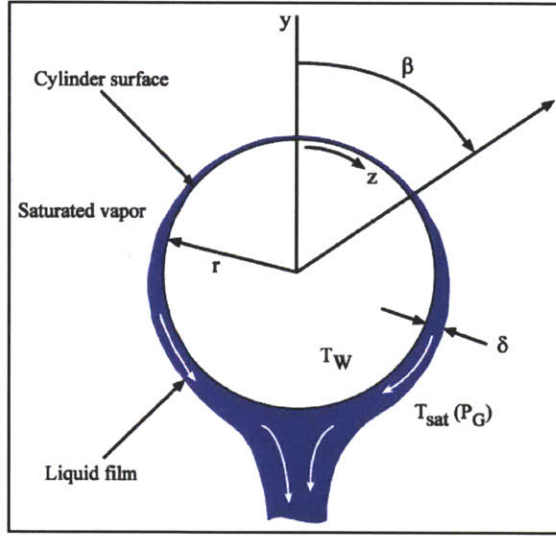


Figure 2.1: Cross-sectional view of condensation along a circular tube [9].

Nusselt integral approach to laminar film condensation on a vertical isothermal plate, the same can be done on a single isothermal tube. The flow is almost always laminar on a single tube due to the short cooling length around the perimeter of the tube as shown in Figure 2.1 [9]. An energy balance can be done between the heat conduction film of thickness δ and the latent heat at the interface [9].

$$h_{L,G} \frac{d\Gamma}{dz} = \frac{k_L [T_{sat}(p_G) - T_w]}{\delta} \quad (2.1)$$

Using a momentum balance along the circumference of the circular tube and boundary condition of $u = 0$ at $y = 0$ the velocity profile is as follows, as a function of angle β :

$$u_y = \frac{(\rho_L - \rho_G)g \sin \beta}{\mu_L} \left[y\delta - \frac{y^3}{2} \right] \quad (2.2)$$

By integrating this velocity profile, the mass flow rate per unit tube length, Γ , can be obtained:

$$\Gamma = \rho_L \int_0^\delta u_y dy = \frac{\rho_L (\rho_L - \rho_G) g \delta^3 \sin \beta}{3\mu_L} \quad (2.3)$$

Substituting this equation into Equation 2.1 and integrating from the top of the tube $\beta = 0, \Gamma = 0$ to the bottom of the tube $\beta = \pi, \Gamma = \Gamma$ a relationship for mass flow rate per unit tube length on one

half of the tube can be derived:

$$\Gamma = 1.924 \left[\frac{r^3 k_L^3 (T_{sat} - T_w)^3 (\rho_L - \rho_G) g}{h_{L,G}^3 v_L} \right] \quad (2.4)$$

Another energy balance on the circumference of the tube is done in order to obtain the mean heat transfer coefficient for the perimeter of the tube:

$$2h_{L,G}\Gamma = 2\pi r h_f (T_{sat} - T_w) \quad (2.5)$$

where h_f is the mean heat transfer coefficient. Substituting Equation 2.3 into the above energy balance we obtain the mean heat transfer coefficient:

$$h_f = 0.728 \left[\frac{\rho_L (\rho_L - \rho_G) g h'_{L,G} k_L^3}{D \mu_L (T_{sat} - T_w)} \right]^{1/4} \quad (2.6)$$

where D is the outside tube diameter. This yields Nusselts correlation for condensation on horizontal tubes:

$$Nu_D = 0.728 \left[\frac{\rho_L (\rho_L - \rho_G) g h'_{L,G} D_L^3}{\mu_L k_L (T_{sat} - T_w)} \right]^{1/4} \quad (2.7)$$

By analytically deriving the heat transfer coefficient with the Nusselt theory, the heat transfer rate of the condensing tube can be predicted by a simple energy balance. This prediction is used to compare with the experimental filmwise results for validation purposes. Additionally, the Nusselt model will be used to compare with the results in the dropwise condensation experiments.

2.2 Experimental Heat Transfer Model

For the experiments at hand, the model used consists of a single tube with cold water running through the inner diameter as the outside diameter is exposed to the saturated environment. The model is depicted in Figure 2.2. The temperature of the environment is kept at a constant T_{sat} as the temperature of the water inside the tube increases exponentially producing a temperature gradient, which simultaneously produces a heat transfer rate.

In order to calculate the heat transfer of this model we use a simple energy balance on the tube relating the inlet and outlet temperatures [10]:

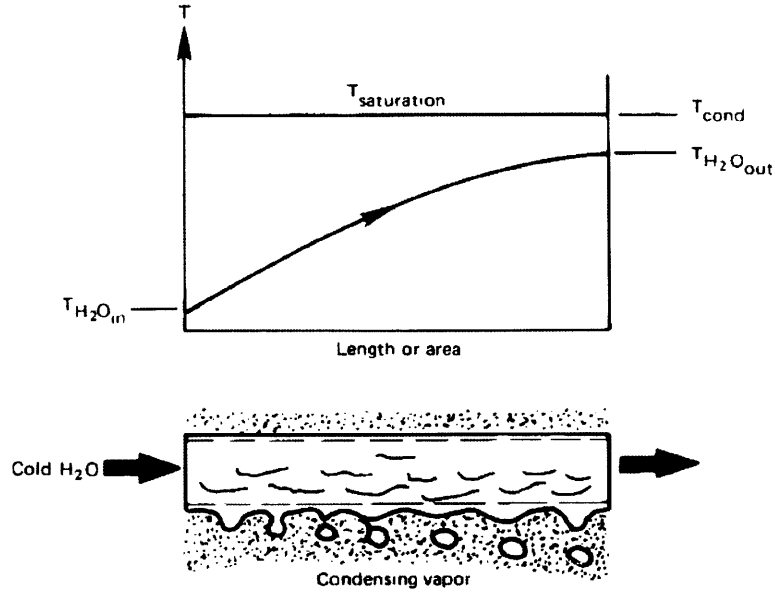


Figure 2.2: Condensing vapor along outer tube with water at inlet and outlet. Temperature profile along the tube increases exponentially [10].

$$\dot{Q} = \dot{m}c_p(T_{out} - T_{in}) \quad (2.8)$$

where \dot{m} is the flow rate inside the tube. To derive the heat transfer coefficients for this model we do an energy balance relating Equation 2.8 and the log mean temperature difference (LMTD), ΔT_{mean} .

$$\dot{m}c_p(T_{out} - T_{in}) = UA\Delta T_{mean} \quad (2.9)$$

$$U = \frac{\dot{m}c_p(T_{out} - T_{in})}{A\Delta T_{mean}} \quad (2.10)$$

where U is the overall heat transfer coefficient of the tube and A is the surface area of the outer diameter of the tube since the temperature drop across the thickness of the tube is neglected. The appropriate ΔT_{mean} for use in this model is the following:

$$\Delta T_{mean} = LMTD = \frac{(\Delta T_a) - (\Delta T_b)}{\ln(\frac{\Delta T_a}{\Delta T_b})} \quad (2.11)$$

where $\Delta T_a = T_{sat} - T_{water,out}$ and $\Delta T_b = T_{sat} - T_{water,in}$. With this model, heat transfer comparisons were made amongst the dropwise and the filmwise condensation samples.

Chapter 3

Experimental Setup, Configuration and Procedures

For initial analysis of the fabricated aluminum surfaces that were studied, condensation experiments were first done using optical microscopy where the samples lay on a cold stage while under the presence of humidified nitrogen gas. With these initial results, it was determined whether or not the aluminum surfaces would exhibit proper superhydrophobic condensation. The onset of nucleation was observed as well as the coalescence behavior of the condensed droplets on the aluminum samples. The setup for these experiments is discussed in the preceding section and the results are discussed in the latter.

The presence of non-condensables has played a significant role in condensation experiments being the main source for the decrease in heat transfer performance. One of the primary goals of the present study was to conduct condensation experiments in an environment with a minimal concentration of non-condensables. In order to do so, a large, high quality environmental chamber was custom designed and built. This chamber would help in decreasing the non-condensable concentration, reducing pressure fluctuations within the chamber due to its relatively large volume, and facilitate experiments by keeping the experiments contained.

3.1 Optical Microscopy Condensation Setup

The synthesized aluminum samples were observed using a high resolution CMOS camera (Phantom v7.1, Vision Research), with a 40x lens, while being cooled from the back side by a cold stage (Instec, TS102-00) set at 10 °C and under a humidified nitrogen vapor environment. The humidified

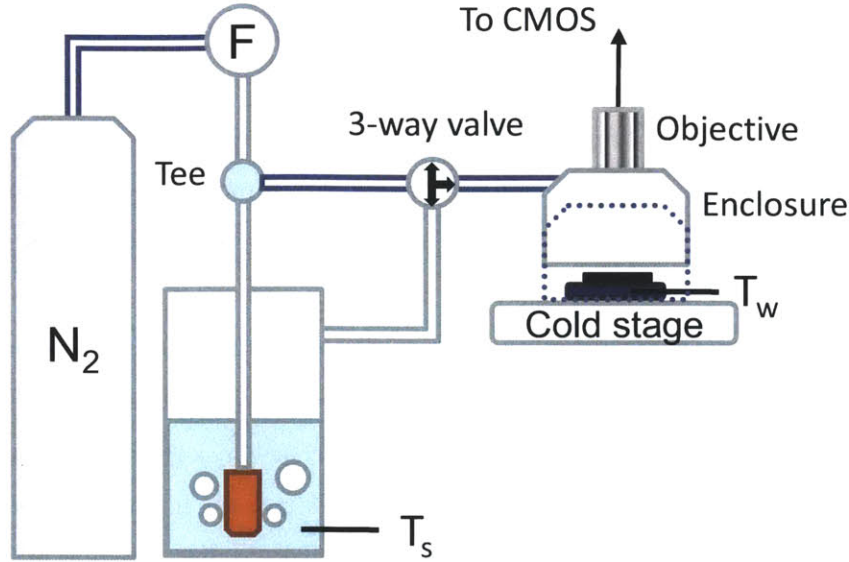


Figure 3.1: Schematic of setup used for initial condensation experiments.

nitrogen vapor was created by letting dry nitrogen bubble through a heated water reservoir set at 25 °C and then to the sample surface. A by-pass valve was installed to provide the delivery of dry nitrogen gas to the sample as it was being cooled to the test temperature at the beginning of each experiment. Figure 3.1 displays the setup for these initial condensation experiments. Good thermal contact between the sample and the cold stage was ensured by interposing a thin layer of thermal grease (Omegatherm, Omega) with a thermal conductivity of 2.2 W/m.K. The samples were covered with an enclosure to ensure there was minimal leakage of the humidified nitrogen gas.

3.2 Environmental Chamber and Sample Setup

The environmental chamber used for this study was custom designed and was supplied by Kurt J. Lesker. The chamber is made of stainless steel with a door sealed with a rubber gasket, two viewing windows, and apertures for various components. Resistive heater lines were wrapped around the exterior of the chamber walls to prevent condensation at the inside walls and the chamber was wrapped with insulation on the exterior walls. The output power of the resistive heater lines was controlled by a voltage regulator. Two short stainless steel water flow line tubes were welded onto the

chamber wall which were connected to insulated rubber hoses that were attached to a water pump (Neslab). A flow meter (Hedland) was integrated along the water inflow line. The water pump was connected to an external water source that constantly supplied chilled water. Another stainless steel tube line was welded onto the chamber wall that served as the flow line for the incoming water vapor that came from a steel water vapor reservoir; this line was wrapped with a rope heater and controlled by a voltage supply. This reservoir was wrapped around with a rope heater and insulation. Two valves were connected to the water vapor reservoir: one led to ambient for use in filling the reservoir with water and the other led to the chamber to control vapor inflow. K-type thermocouples were allocated along the length of the water vapor reservoir to monitor temperature differences along the reservoir. A bellows valve was attached to the chamber to serve as a link between the inner chamber and ambient. In order to monitor temperatures within the chamber, k-type thermocouple bundles were connected through the chamber apertures. A pressure transducer was attached to monitor pressures within the chamber. The thermocouple bundles and the pressure transducer were both linked to an analog input source (National Instruments) which was connected to the computer in order to record and store data. Another bellows valve was integrated onto the chamber that led to a vacuum pump which was used to pump the chamber down to vacuum conditions. A liquid nitrogen reservoir was incorporated along the line from the chamber to the vacuum which served to remove any moisture from the pump-down process and ultimately assist in yielding higher quality vacuum conditions. A bellows valve was also integrated from the vacuum pump and liquid nitrogen reservoir lines to ambient in order to slowly release the nitrogen line to ambient conditions. In order to visually record data, a high speed camera (Phantom v7.1, Vision Research) was placed aside one of the viewing windows on the chamber. The entire schematic of the exterior of the environmental chamber is depicted in Figure 3.2 and the actual configuration of the chamber, used during experimentations, is shown in Figure 3.3 and Figure 3.4.

The setup that was used to run experiments inside the chamber is depicted in Figure 3.5. Stainless steel bellows tube lines were connected to the external water flow lines and onto Swagelock T-connections. K-type thermocouple probes were connected to the T-connection using Ultra-Torr vacuum adapters. The sample, consisting of a 6.35 mm diameter tube, was connected to a Swagelock fitting onto the T-connection. Chilled water would flow through the inlet bellows tube, along the

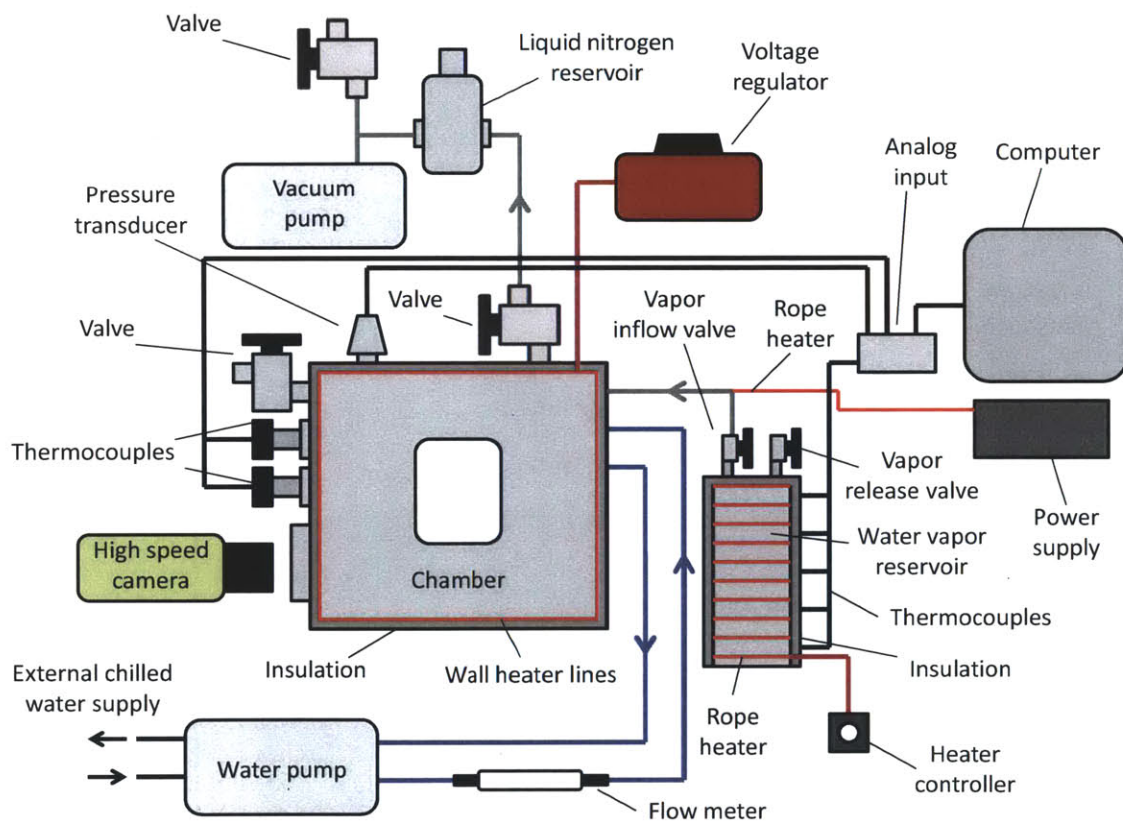


Figure 3.2: Schematic of environmental chamber setup.

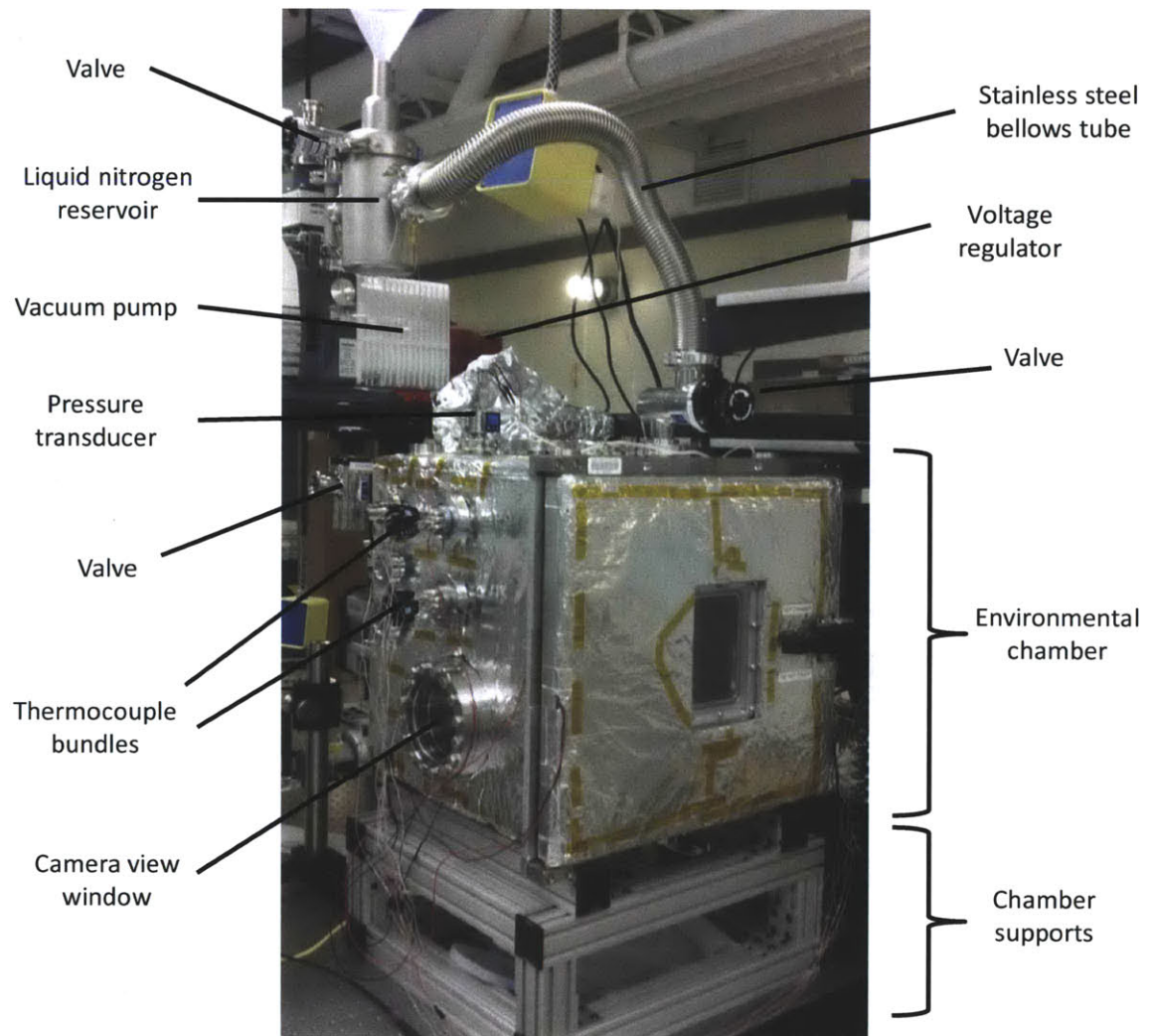


Figure 3.3: Front view configuration of environmental chamber.

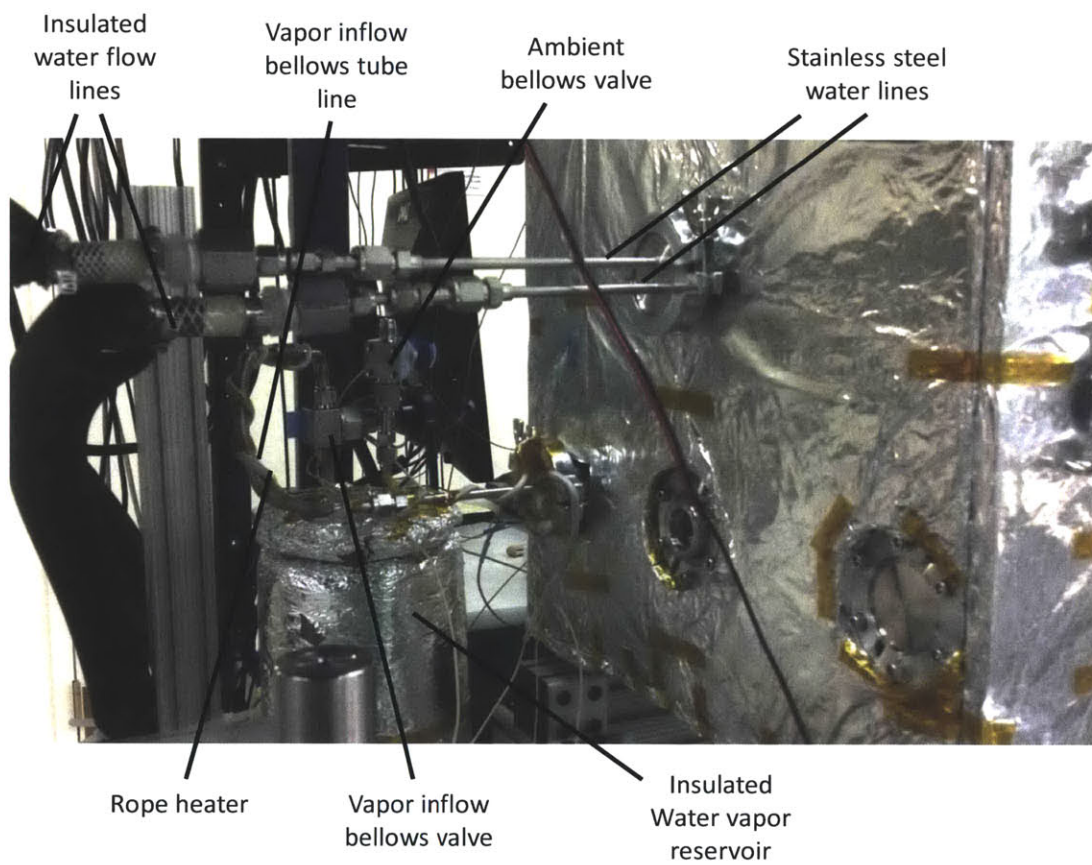


Figure 3.4: Back view configuration of environmental chamber.

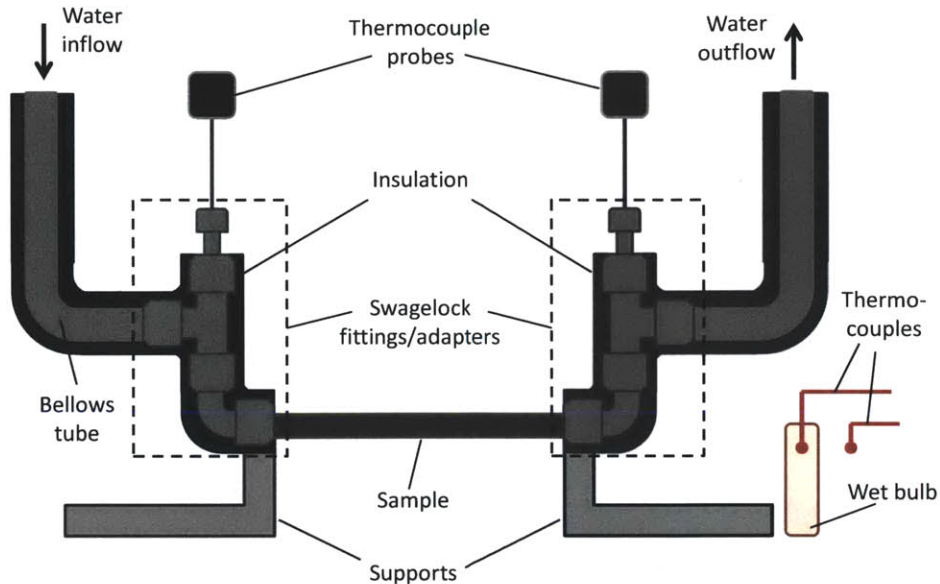


Figure 3.5: Sample setup for condensation experiments.

inside of the tube sample and through the outlet. Two supports were used to hold the sample and the entire configuration in place. A wet bulb was placed beside the sample and was made by embedding a k-type thermocouple in a thin piece of fiberglass insulation that reached the base of the chamber to wick up water from the bottom of the chamber to keep the thermocouple bead wet. Another thermocouple was placed beside the sample in order to measure the reference temperature inside the chamber; this served as the dry bulb temperature measurement. As the trials progressed, the wet bulb would get wet from the condensate building up inside the chamber and its temperature was compared to the reference temperature inside the chamber. This allowed for the relative humidity within the chamber to be measured.

3.3 Optical Microscopy Experimental Procedures

The procedures for the optical microscopy condensation experiments were straight forward. The temperature controlled cold stage was set to a temperature of 10°C . During this cool-down process of the stage, dry nitrogen was being delivered to the sample. Once the temperature of the stage was stable, the by-pass valve was closed to initiate the flow of the water-saturated nitrogen gas to the

sample enclosure. Simultaneously, the visual recording was initiated in order to record the onset of nucleation. The trials took approximately 20 min each. While the experiments ran, the objective was constantly being refocused in order to capture the best image of the sample during droplet growth and coalescence.

3.4 Environmental Chamber Experimental Procedures

For every experimental trial using the environmental chamber, a set of procedures/guidelines were set in order to keep consistency throughout the experiments. The first step of the process was to turn on the voltage regulator that heats up the environmental chamber walls, which prevented condensation inside the wall surfaces. Simultaneously, the water vapor reservoir was filled with approximately 1.5 liters of DI water using a syringe through the vapor release valve. After opening the vapor inflow valve and closing the vapor release valve, the rope heater around the water vapor reservoir was turned on with the heater controller to max capacity and the rope heater connected to the vapor inflow valve was also turned on. The temperature of the water reservoir was monitored with the installed thermocouples; the temperature at the top of the reservoir was higher than that of the middle/bottom of the reservoir due to the water thermal-mass present at the middle/bottom section. Hence, it was made sure that the regions of the water reservoir of higher thermal capacity were brought to a sufficiently high temperature to enable boiling. During the boiling process, aluminum foil was placed on the bottom surface of the inner chamber in order to catch any of the water spitting out from the vapor inflow line. Once the boiling was complete, the vapor inflow valve was closed. The excess water that spilled onto the chamber was drained from the bottom of the chamber through one of the chamber openings.

In order to install the samples onto the condensation sample rig, in Figure 3.5, the Swagelock adapters at the ends of the tube samples were connected to the 90 degree elbow Swagelock connectors on the rig. Before installing the entire sample setup in the chamber, all adapters/connectors were tightened to ensure that there were no leaks which may affect vacuum performance. The setup was then placed on top of the steel supports and the bellows tubes, for the water inflow/outflow, were connected to the water lines and the Swagelock fittings were tightened. Afterwards, the wet bulb was placed near the sample touching the bottom surface of the chamber and then the chamber was closed.

The next step was to begin the vacuum pump-down procedures. Initially, the liquid nitrogen reservoir was filled with liquid nitrogen to about half the volume of the reservoir. The ambient

exposed valves connecting the chamber and the vacuum pump were both closed and the valve connected to the liquid nitrogen reservoir was opened. The vacuum pump was then turned on initiating the pump-down process. The pressure inside the chamber was monitored during the pump-down process; this process took several hours in order to achieve adequate vacuum conditions. Once high quality vacuum conditions were achieved, the valve connected to the liquid nitrogen reservoir was shut and the vacuum pump was shut off.

The proceeding steps involved setting up the water loop-flow. The Neslab water pump reservoir was filled and turned on to a flow rate of 2 L/min; the flow rate was monitored with the flow meter integrated in the inflow water line. In order to bring the chilled water into the flow loop, the external chilled water lines were opened; this allowed for the circulation of chilled water through the tube sample.

To begin the experiments, the Phantom camera was turned on for visual recording of the sample during condensation; the software was set for recording data. Afterwards, the rope heater around the water reservoir was turned off and the vapor inflow valve was slowly turned open until the pressure read 20 MPa. The experiment was set to run at these conditions for a certain time period. After successful recording at these conditions, the pressure level was increased by opening the vapor inflow valve; this increased the saturation temperature inside the chamber. The pressure inside the chamber was increased periodically in order to obtain the heat transfer rate results that will be presented in the latter.

Chapter 4

Aluminum Sample Synthesis, Preparation and Characterization

One of the primary goals of the present study was to develop a synthesis procedure for aluminum surfaces that can be done with ease and in a timely fashion. Two surface fabrication methods were studied on aluminum substrates. The first procedure involved a simple chemical etch process using hydrochloric acid to produce microscale features at the grain boundary of the aluminum. The second procedure was done through an oxidation process using sodium hydroxide producing rough micropatterns on the surface of the aluminum. A third surface was made by combining the two prior processes; the aluminum samples were first chemically etched and then oxidized.

4.1 Sample Synthesis and Preparation Procedures

Initially, all the synthesis processes were done on aluminum square specimens. These squares were cut in 2x2 cm from a commercially available aluminum sheet of 0.025" thickness. Before any synthesis procedures, the square samples went through a cleaning procedure. The samples were first put in a beaker containing trichloro ethylene and placed in the ultrasonicator for 15 minutes for a degreasing process. Afterwards, the samples were rinsed with DI water and dried with dry nitrogen.

The surface preparation for the aluminum hydrochloric acid etching was based on the synthesis procedure developed by Y. Zhijia et. al. [12]. The samples were immersed in beakers containing hydrochloric acid of 4 M concentration at room temperature under a vent hood. Three different etch times were conducted, 12 min, 16 min, and 20 min with two samples in at each etch time. After etching, the specimens were immediately rinsed with DI water and dried with dry nitrogen.

The preparation procedures for the oxidized aluminum surfaces with sodium hydroxide were based on the novel process by N. Saleema *et. al* [7]. The aluminum squares were immersed in beakers containing sodium hydroxide of 0.4 M concentration at room temperature. The oxidation process was done for different times between 5-20 minutes. After the oxidation process, the specimens were rinsed with DI water and dried with dry nitrogen.

For further exploration, a hybrid aluminum surface preparation was made using the acid etch and the oxidation. The aluminum square samples were first etched with the 4 M concentrated hydrochloric acid for 4 minutes and then rinsed and dried. Next, these samples were immersed in the 0.4 M concentrated sodium hydroxide solution for three different times, 10, 15, and 20 minutes. The samples were then rinsed with DI water and dried with dry nitrogen.

After the samples all had time to dry in air, the samples were placed inside a plasma cleaner (Har-rick Plasma, PDC-002) for about 1 hour at 400 Torr. Afterwards, the samples were functionalized with silane to serve as the low surface energy coating that gave the samples their superhydrophobic behavior. Each sample was placed inside a desiccator with a petri dish of trichloro (1H, 1H, 2H, 2H perfluorooctyl) silane (TCS) under vacuum conditions for approximately 50 minutes. The samples were then removed and left to rest over night.

To prepare the surfaces on the circular tubes, a couple of different approaches were taken. Aluminum tubes of 6.25" length were cut from a commercially available aluminum tube with an outer diameter of 6.35 mm and an inner diameter of 3.65 mm. The tubes were then capped at both ends with 0.25" Swagelok end caps which avoided any leaking inside the tube during the surface preparation. For the cleaning procedure, the tubes were immersed in acetone for 10 minutes to remove all the organic impurities. Afterward, in order to remove the natural oxide present on the surface, the tubes were dipped into a 2 M solution of hydrochloric acid for 15 minutes. The tubes were then synthesized in the same manner as the square samples, but were immersed in graduated cylinders rather than beakers. The etch times in the HCl samples was reduced to 7-8 minutes of etch time in order to avoid etching through the tube walls. Afterward, the samples were functionalized using TCS.

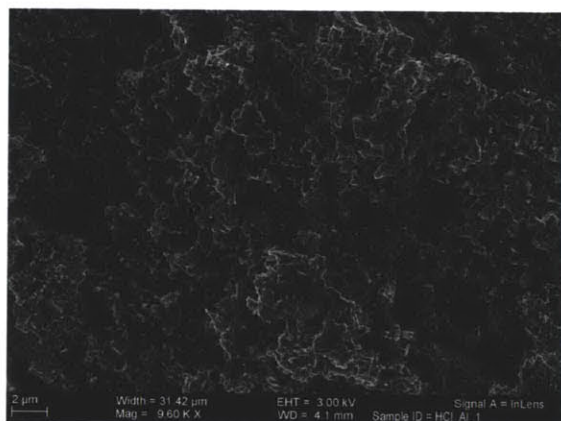
To serve as a baseline for the experiments, filmwise and smooth dropwise tube samples were also prepared. The aluminum tubes were cleaned in a similar fashion as the prior with acetone and 2 M HCl. The dropwise sample was immersed into a graduated cylinder containing hydrogen peroxide for 10 minutes and then rinsed with DI water and dried with dry nitrogen. Both samples were put into the plasma cleaner for approximately one hour once they were fully dried. The dropwise sample was then functionalized with silane using the same functionalization procedure as before.

4.2 Sample Characterization

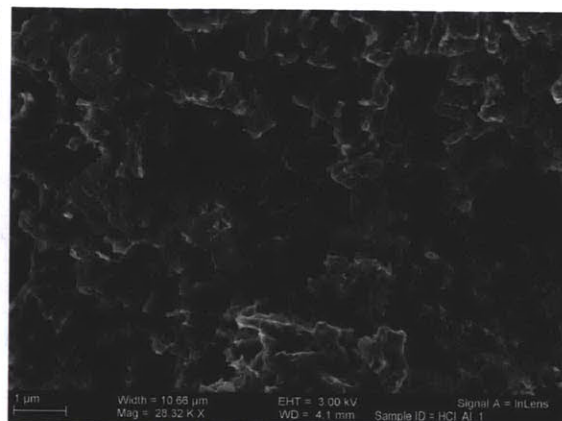
A field emission scanning electron microscope (FESEM) was used to obtain images of the synthesized aluminum surfaces. Figure 4.1 displays the FESEM images of the HCl etched aluminum sample with an etch time of 12 min at varying magnifications. From the images, etch pits are formed from the etching process. These etch pits take place at the dislocation sites of the aluminum surface. The surface yields a very rough hierarchical composition with rectangular-like structures. There appear to be many levels of features due to the etching process. This gives the surface these hierarchical steps with very sharp, jagged features. Figure 4.2 depicts the FESEM images of the HCl etched aluminum sample with an etch time of 16 min at varying magnifications. The features of the 16 min etched surface are very similar to that of the 12 min etched sample. However, for the 16 min etched sample the feature sizes are much smaller and more refined due to the longer etch time. The jagged, step-like structures are really clear in this sample and more uniform throughout the sample as well. In 4.2a there is an etch pit due to the strongly concentrated HCl etch recipe.

Figure 4.3 depicts the FESEM images of the NaOH oxidized aluminum sample with a 15 min oxidation time. From the oxidation, the samples develop a layer of oxide which is apparent in Figure 4.3a. There are areas of non-uniformity in oxidation which leaves some gaps of unoxidized aluminum as seen in Figure 4.3a; this non-uniformity creates segmenting along the surface. At higher magnifications, there are these sharp, needle-like features on the surface of the oxide. The surface yields mountain-like features with the needle-like structures at the top. Figure 4.4 displays the hybrid sample with an HCl etch time of 4 min and an NaOH oxidation time of 20 min. The HCl etch creates the etch pits seen in figure 4.4a; the dark spot are the pits due to the acid etch. In Figure 4.4b, the hierarchical steps from the HCl etch can be seen; the surface has multiple levels of structures from the acid etch process. However, the sharp, jagged features seen in the HCl etched samples from before are not apparent in the hybrid sample because the oxide covers these features. Instead, a layer of oxide is formed on top of the etched aluminum and the oxide creates the same needle-like features on the surfaces of the etched aluminum.

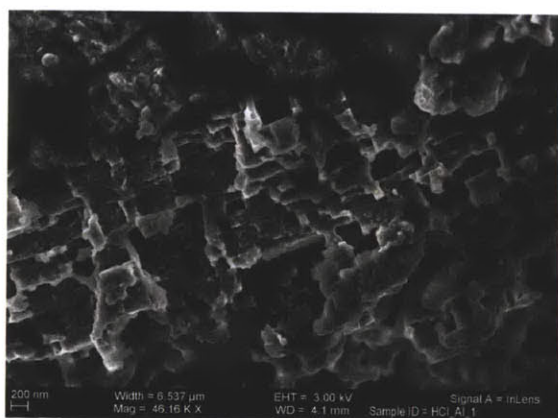
During the FESEM imaging session, there were areas on the sample with high concentration levels of silane deposit. Some of these areas developed large silane concentrations and formed blobs and thick coatings. The silane is supposed to deposit as a monolayer on the microstructures, however, in some areas of the samples the silane deposit was substantially greater than that of a monolayer. These images can be seen in the Appendix. This could have been due to improper procedures of silane deposition, such as rinsing the samples immediately after the silane deposition process.



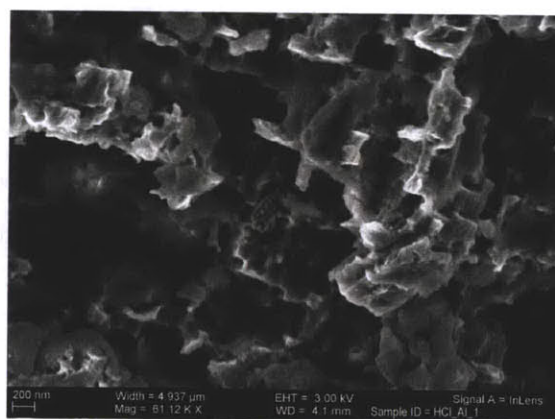
(a)



(b)



(c)



(d)

Figure 4.1: FESEM images of aluminum HCl 12 min etch at (a) 9600, (b) 28320, (c) 46160, (d) 61120 magnifications.

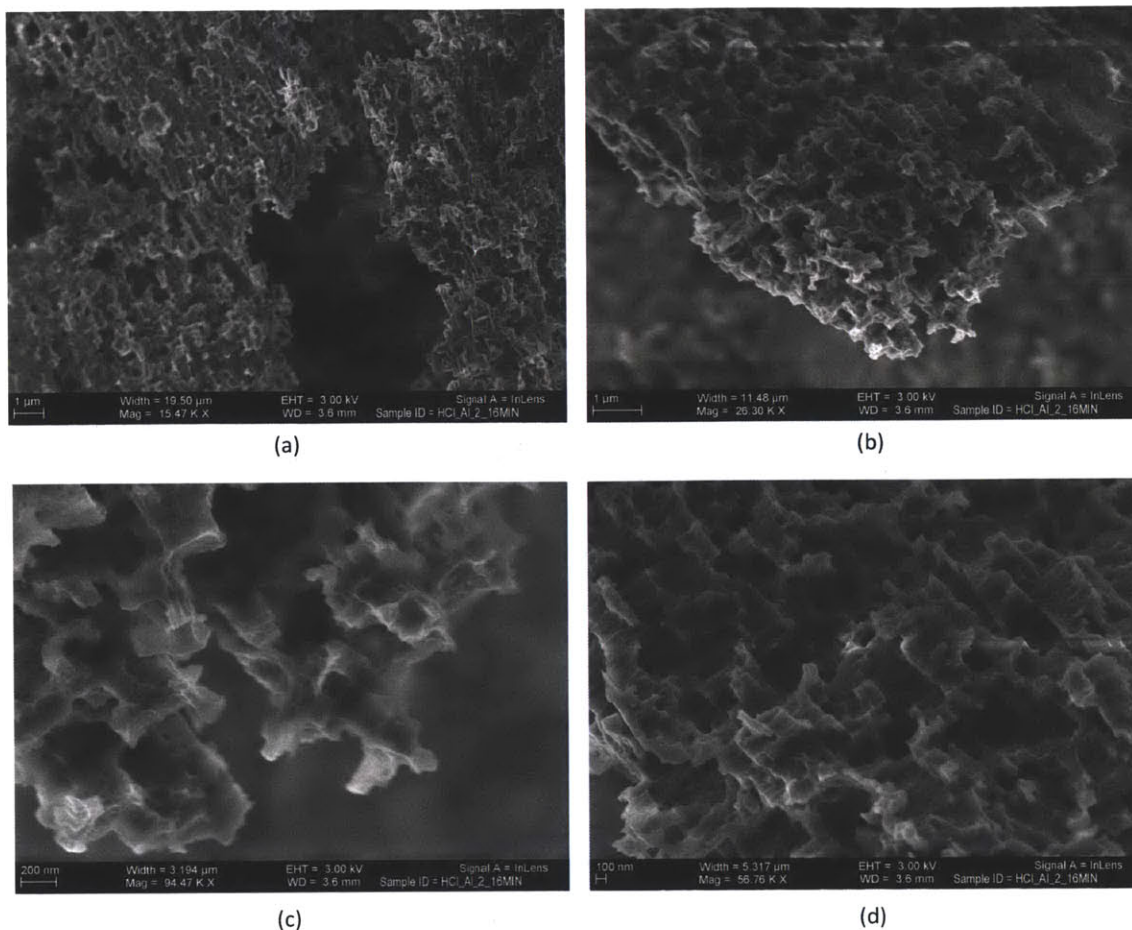


Figure 4.2: FESEM images of aluminum HCl 16 min etch at (a) 15470, (b) 26300, (c) 94470, (d) 56760 magnifications.

Contact angle measurements of the samples were made using an automatic microscopic contact angle meter (Kyowa Interface Science Co. LTD., MCA-3). The images shown in Figure 4.5 show typical droplet wetting behavior on the functionalized aluminum samples: 1. the 16 min HCl etched sample, 2. the 15 min oxidized NaOH sample, 3. the hybrid sample of 4 min HCl etch and 20 min NaOH oxidation. Upon performing the contact angle measurements, the roughness of the surfaces made it difficult for the automatic microscopic contact angle meter to obtain precise results consistently; the meter's algorithm failed to recognize the reflection line of the samples in much of

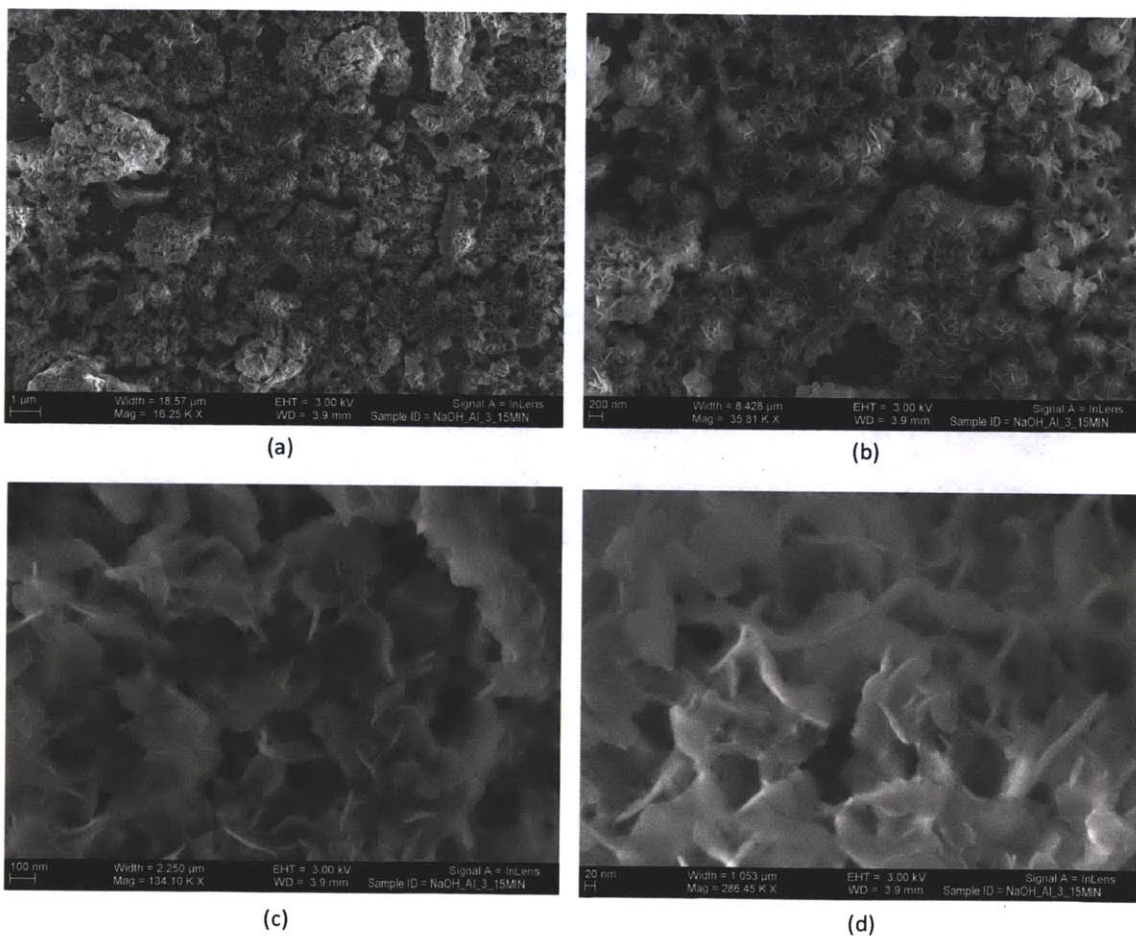


Figure 4.3: FESEM images of aluminum NaOH 15 min oxidation time at (a) 16250, (b) 35810, (c) 134100, (d) 286450 magnifications.

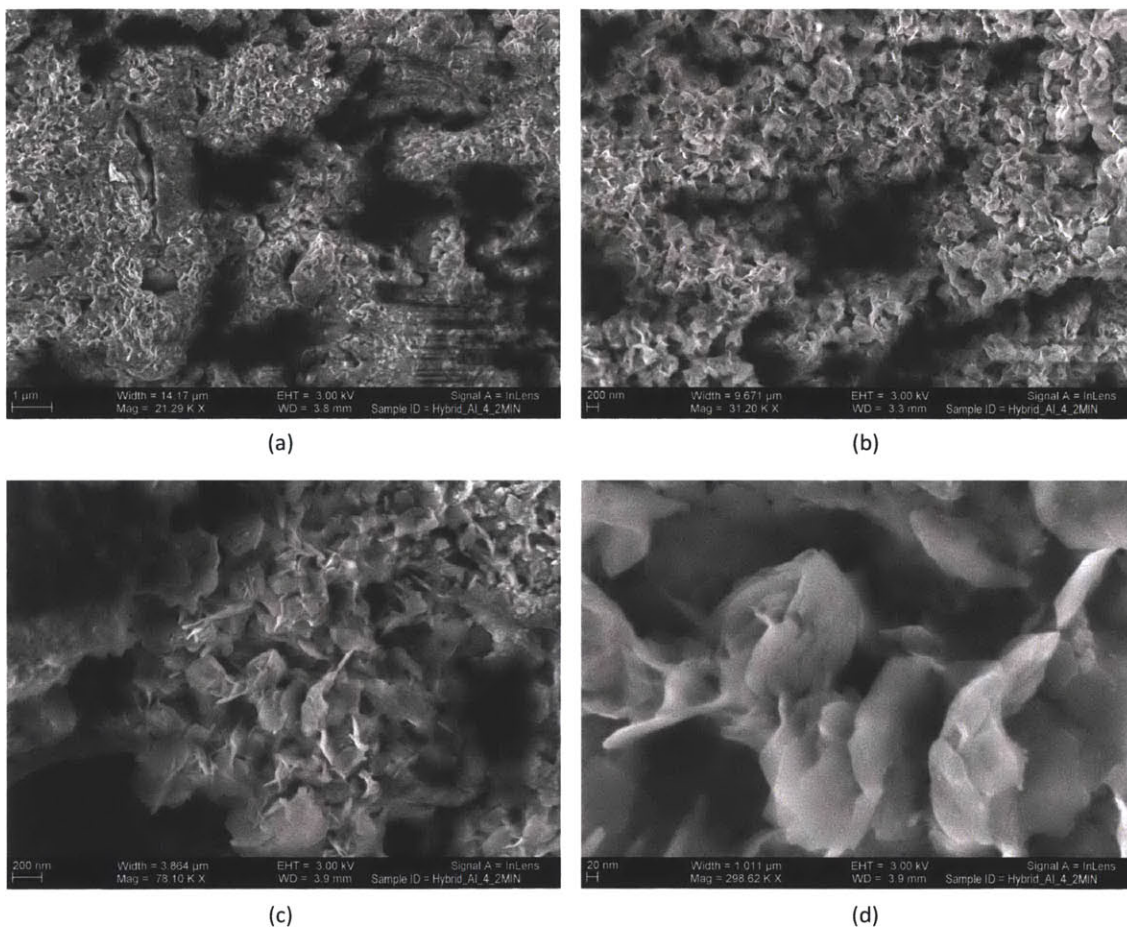


Figure 4.4: FESEM images of aluminum hybrid sample of 4 min HCl etch and 20 min NaOH oxidation at (a) 21290, (b)31200, (c)78100, (d)298620 magnifications.

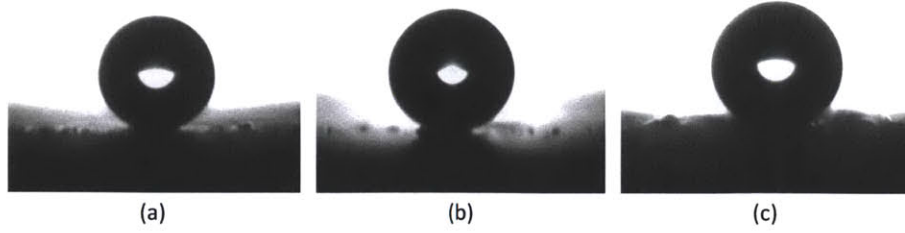


Figure 4.5: Equilibrium contact angle measurement images. (a) HCl 16 min etch, (b) NaOH 15 min oxidation time, (c) hybrid surface 4 min HCl etch, 20 min NaOH oxidation.

Sample	Equilibrium Contact Angle	Receding Contact Angle	Contact Angle Hysteresis
HCl	$162.4^{\circ} \pm 0.1^{\circ}$	$157.0^{\circ} \pm 0.1^{\circ}$	$5.4^{\circ} \pm 0.1^{\circ}$
NaOH	$164.1^{\circ} \pm 0.1^{\circ}$	$159.5^{\circ} \pm 0.1^{\circ}$	$4.6^{\circ} \pm 0.1^{\circ}$
Hybrid	$163.3^{\circ} \pm 0.1^{\circ}$	$158.6^{\circ} \pm 0.1^{\circ}$	$4.7^{\circ} \pm 0.1^{\circ}$

Table 4.1: Measured Contact angles for three aluminum samples.

its recording. The hybrid sample was the most difficult to obtain contact angle results for due to its high roughness factor from the etch and oxidation processes; this can be seen in Figure 4.5c. The feature scales of these samples are in the order of magnitude of approximately 100 microns.

Table 4.1 depicts the equilibrium and receding contact angle measurements of the three surfaces. The surfaces exhibited contact angles of greater than 160° giving them their hydrophobic attribute. The contact angle hysteresis for each of the surfaces was about 5° .

Chapter 5

Experimental Results and Discussion

With the optical microscopy condensation experiments, it was determined that the synthesized aluminum surfaces did not exhibit the jumping behavior due to the Wenzel morphology of the droplets upon coalescence. The next section will present visual results of the condensation behavior of each surface.

Continuing with the heat transfer experiments in the environmental chamber, temperature data was recorded from the inlet/outlet tube sample ends and from the wet/dry bulb and internal chamber thermocouple readings. Using the temperature data and the experimental models presented in section 2, the heat transfer rates of the condensation experiments were analyzed. In the latter section, the heat transfer results for the filmwise, dropwise, and HCl etched superhydrophobic aluminum surfaces will be presented and explained.

5.1 Optical Microscopy Condensation Analysis

From these experiments, nucleation observations were made in order to understand the behavior of the droplets at the onset of nucleation. Additionally, the growth and coalescence behavior of the droplets were observed at latter times in the runs. The images in Figure 5.1 depict the onset of nucleation and the coalescence/growth behaviors of three samples: 1. the 12 min HCl etched sample, 2. the 15 min oxidized NaOH sample, 3. the hybrid sample of 4 min HCl etch and 20 min NaOH oxidation. From the visual results, the surfaces all exhibited similar growth and coalescence behaviors.

At the onset of nucleation, the HCl and hybrid samples exhibited high levels of nucleation density, as can be seen in the figures. The approximate nucleation density for these two surfaces was in the order of $10^{10} \text{ sites/m}^2$. The NaOH sample appeared to have only a region of populated nucleation sites while the rest remained absent of nucleation sites; this was perhaps due to the quality of coverage of the silane coating. At low supersaturations, $S \sim < 2.5$, water does not nucleate on silane; this is indicative that the silane may not have been deposited on the NaOH oxidized surface properly, hence leaving the underlying exposed oxide microstructures to provide nucleation sites because of their wettability.

Towards the beginning of the growth process, some droplets appear to be growing in the Wenzel state, beyond the transition point, $E^* > 1$; this can be seen from the images in the first column in Figure 5.1 where some of the droplets are darker in complexion. Upon coalescence, the light reflects giving these droplets their lighter color indicating the presence of a liquid/vapor interface leading to the Cassie-Baxter wetting state. After coalescence, the wetting transition phase occurs and the droplets begin to slowly go back to their original wetting state in the Wenzel regime. Towards the end of the runs, the larger droplets appeared to be pinned to the surface, thus remaining in the Wenzel regime; this can be seen in the figures on the second column. Additionally, there was an absence of jumping behavior of the droplets; the droplets did not build up enough kinetic energy to jump upon coalescence with neighboring droplets. This suggests that there was a significant contact line pinning at the surface of the microstructures. This conclusion delineated that the surface micro-structures did not exhibit the adequate length scales and morphology to promote the jumping behavior which would further enhance heat transfer during condensation [3]. Hence, these surfaces did not fulfill the scale-invariant wetting energy criterion that allows for superhydrophobic condensation, which was highlighted in section 1.3.

5.2 Environmental Chamber Condensation Results

Though it was concluded that the proposed aluminum surfaces did not fulfill all the requirements for being adequate superhydrophobic condensation surfaces, due to their Wenzel behavior during condensation, potential condensation heat transfer enhancements from the application of these surfaces were still explored in the environmental chamber. Three aluminum tube samples were tested in the environmental chamber: 1. the smooth filmwise, 2. the smooth dropwise, and 3. the HCl etched (8 min. etch time) superhydrophobic surface. By following the procedures in section 3.2, the three

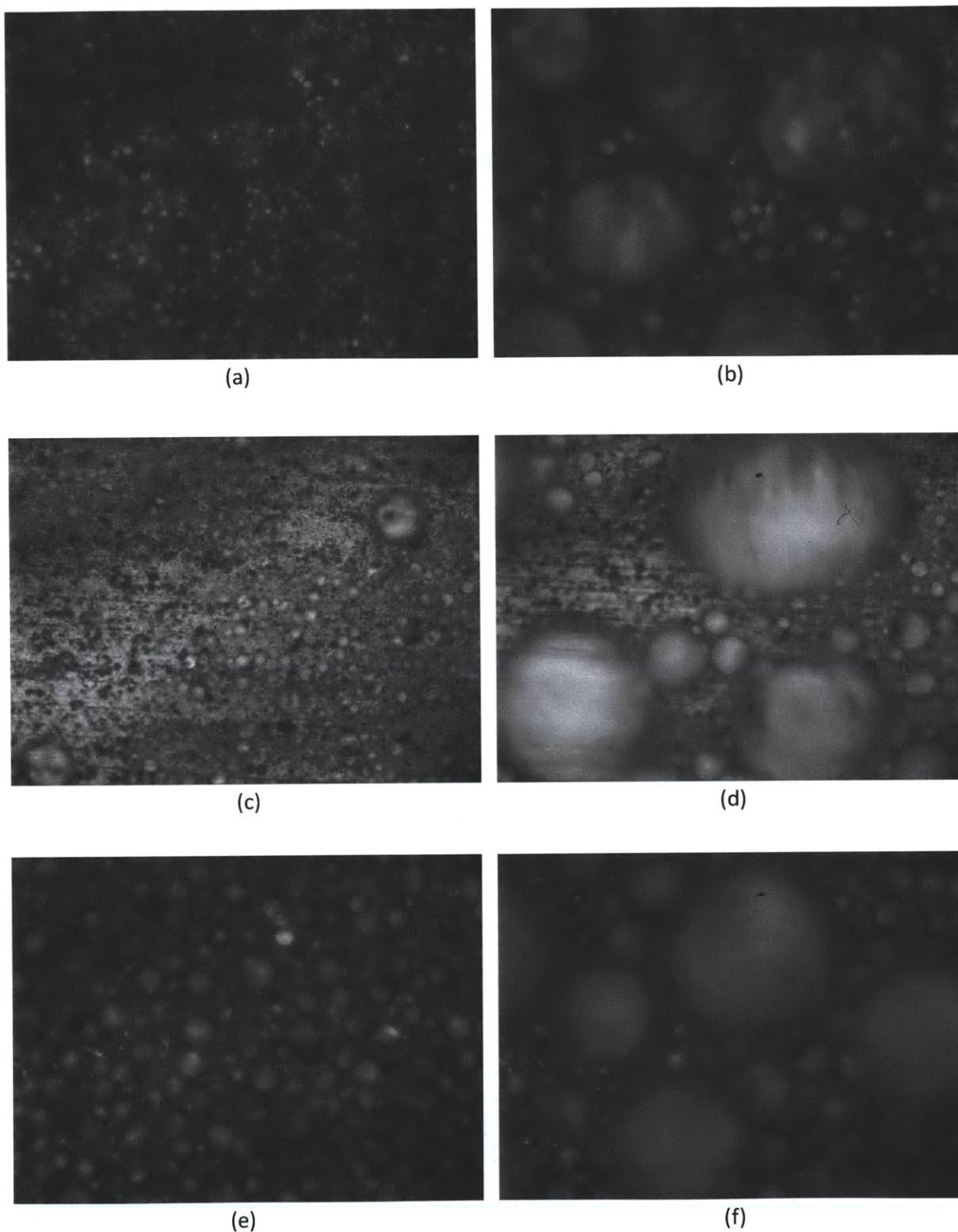


Figure 5.1: Condensation under optical microscopy. (a) onset nucleation HCl 12 min etch, (b) ~ 18 min time-lapse nucleation HCl 12 min etch, (c) onset nucleation NaOH 15 min oxidation time, (d) ~ 18 min time-lapsed nucleation NaOH 15 min oxidation time, (e) onset nucleation hybrid surface 4 min HCl etch, 20 min NaOH oxidation, (f) ~ 18 min time-lapse nucleation hybrid surface 4 min HCl etch, 20 min NaOH oxidation

surfaces were tested under vacuum conditions inside the chamber. The results of the experiments are presented in Figure 5.2; the vertical axis depicts the heat flux in kW/m^2 and the horizontal axis represents the superheat of the system, i.e. the difference between saturation temperature and tube wall temperature. From the graphs it is demonstrated that the heat flux increases with increasing supersaturation inside the chamber in a linear fashion.

From the results presented in the graphs in Figure 5.2a, the Nusselt filmwise tube theory did not align that well with the experimental data. This was due to the flow rate being too low during the experiments with the filmwise sample which resulted in a lower heat transfer coefficient inside the tube. This low heat transfer coefficient due to flow inside the tube, resulted in a lower heat transfer due to condensation. By comparing the graphs in Figure 5.2, it is immediately apparent that the HCl etched aluminum sample did achieve enhanced heat transfer performance with a maximum heat transfer rate of approximately $180kW/m^2$, at a superheat of 10. The maximum heat transfer rate achieved by the smooth, filmwise sample, at a superheat of 10, was approx. $85kW/m^2$ and the max heat transfer achieved by the smooth, dropwise sample was $110kW/m^2$. By comparison, the HCl etched sample outperformed the filmwise heat transfer by about a factor of 2 and the dropwise sample by a factor of 5/3. These results validate that dropwise condensation exhibits larger heat transfer rates than filmwise condensation. Taking into account the reduced thickness of the tube wall due to the etch process in the analysis, the presence of the micro-structures from the HCl etch did in fact add to the improvement of dropwise condensation, implying that the fabricated surfaces have potential for increasing energy efficiency on condensation systems. To confirm the previous condensation experiments done using optical microscopy, jumping behavior was not observed during the experiments with the etched aluminum tube inside the chamber. The condensation droplets along the tube remained in the Wenzel regime throughout the runs.

From observations during the experimental runs, it was noted that flooding of the condensed vapor on the HCl etched tube sample would occur at low supersaturations; the tube exhibited filmwise-like condensation behavior even though the surface was prepared for dropwise condensation. As the supersaturation in the chamber was increased, by increasing the vapor inflow, the flooding gradually dissipated along the tube and dropwise condensation began to dominate, thus giving the results presented in Figure 5.2.

Another important observation that was made during the runs was that the aluminum HCl etched sample appeared to exhibit hydrophobic hysteresis. Essentially, the samples' hydrophobic nature

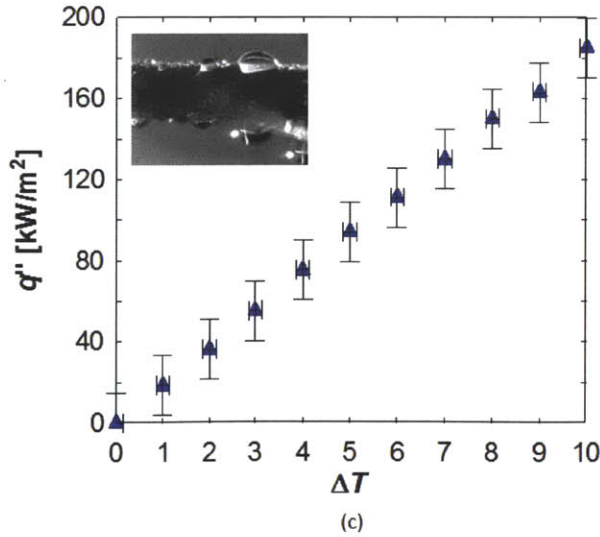
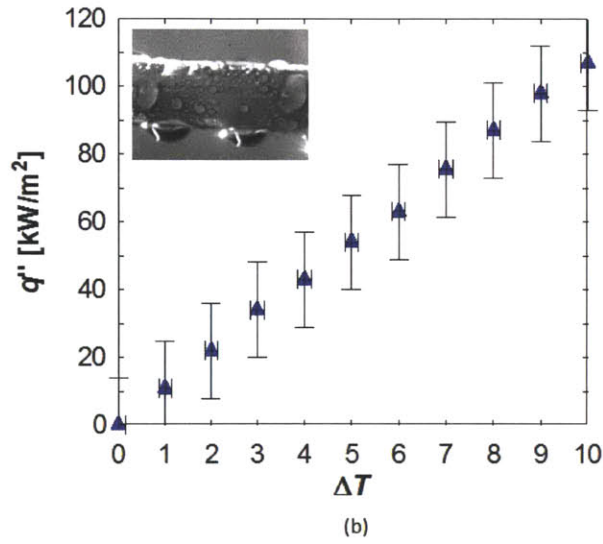
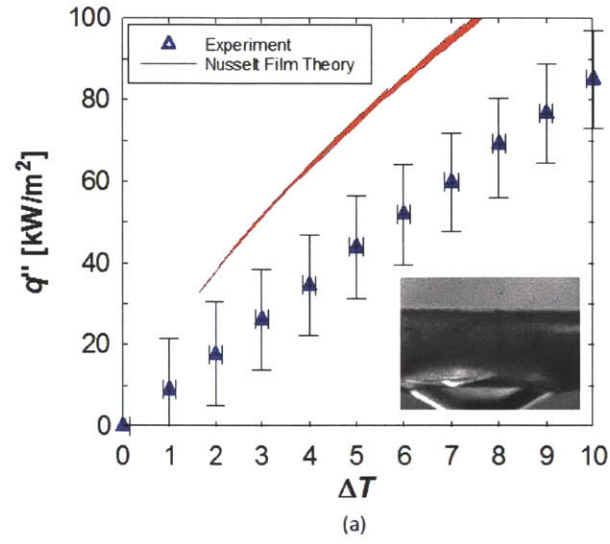


Figure 5.2: Condensation heat transfer results. The heat flux is plotted versus the superheat $T_{sat} - T_{wall}$. (a) results for the smooth, filmwise aluminum surface compared to Nusselt filmwise theory, (b) results for smooth, dropwise aluminum surface, and (c) results for the HCl etched superhydrophobic dropwise aluminum surface.

began to decrease throughout the run; wettability along the tube started to become apparent. This may be due to the long time span of the runs which lasted approximately 8 hrs each. Perhaps during condensation the Wenzel state propagated across the surface during growth which enabled the wetting behavior along the tube walls. A possible solution is to anneal the sample after the silane is deposited in order to refine the structure of the material and make it homogeneous.

Chapter 6

Conclusions and Future Directions

From the results conducted via optical microscopy and in the environmental chamber, it was concluded that the fabricated aluminum surfaces do not allow for the proper wetting transition from the Wenzel energy state to the Cassie-Baxter energy state and achieve a jumping-like behavior which is a necessary criterion for superhydrophobic condensation. However, the HCl etched aluminum surface was able to achieve greater heat transfer rates than the filmwise and smooth, dropwise samples. Therefore, the morphology of the HCl etch on the aluminum was able to promote enhanced heat transfer rates despite the surface being unable to adequately transition to the Cassie-Baxter state.

Further exploration needs to be done using the same surface chemistry but at different acid/oxidation molarities and at different HCl etch and NaOH oxidation times. Essentially, more empirical work must be done with the presented surface fabrication of aluminum in order to see if the surfaces can exhibit dropwise condensation in the Cassie-Baxter regime to achieve the jumping effect during condensation. Perhaps alternative chemicals can be explored to see what types of morphologies can be achieved and if the energy criterion can be satisfied as well.

Though heat transfer was enhanced with the HCl etch, the downside to using the etching process was that it took off a significant amount of native material. In the etch of the 2x2 cm square samples, with etch times ranging from 12-20 minutes, the mass of the samples decreased by 60 to 90% of its original mass. For the aluminum tube samples, with etch times of 7-8 minutes, the mass decreased by 40% of its original mass. Therefore, it is best to look for an alternative fabrication process for superhydrophobic condensation on aluminum surfaces.

One alternative aluminum synthesis processes to explore is anodization on aluminum to form a porous membrane with apertures of nano-scale diameters. Anodization processes allow for narrow pore-size distribution, high-pore density, and thinness [2]. The advantage to this fabrication process

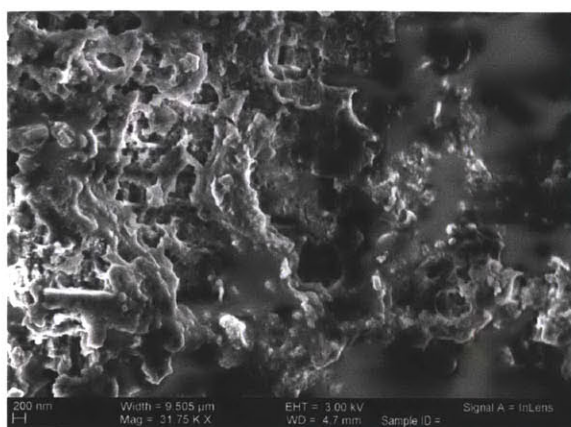
is that the pore size and pore density can be controlled with the anodization voltage, thus a proper superhydrophobic condensation surface morphology can be achieved if the adequate fabrication conditions are set.

Besides condensation applications, an alternate application of these micro-structured aluminum surfaces include icephobic applications. Accretion of ice on surfaces such as aircrafts and network systems is known to cause many problems in the performance of the system. A solution to such problem is to deposit coating materials on the surface to prevent the accumulation of ice on the surface. One example was presented by Saleema *et. al.* who were able to create nanoroughness on aluminum surfaces using a chemical etch followed by 'passivation' of the surface using a Teflon coating [6].

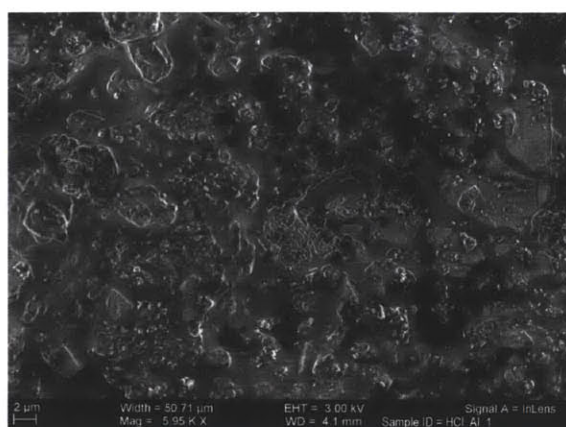
Implementation of such synthesis processes on existing and new systems can, potentially, bring about higher levels of performance in condensation heat transfer and overall energy efficiency. Further exploration must be done to develop a feasible, fast, and low cost fabrication method for aluminum surfaces in order to realize the implementation of this technology to industrial systems.

Appendix A

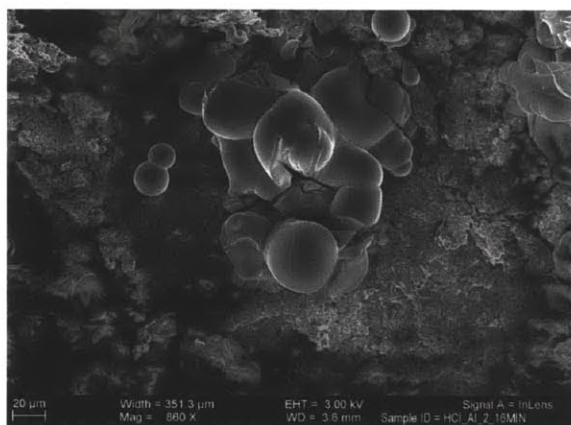
FESEM Images: High Levels of Silane Deposition



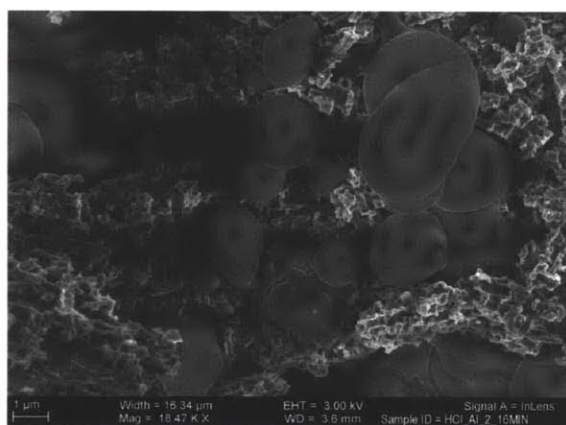
(a)



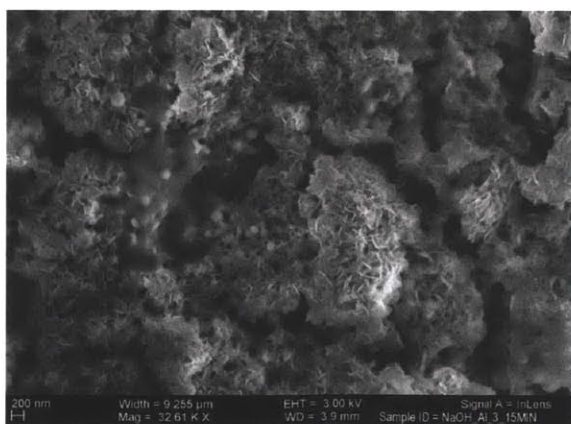
(b)



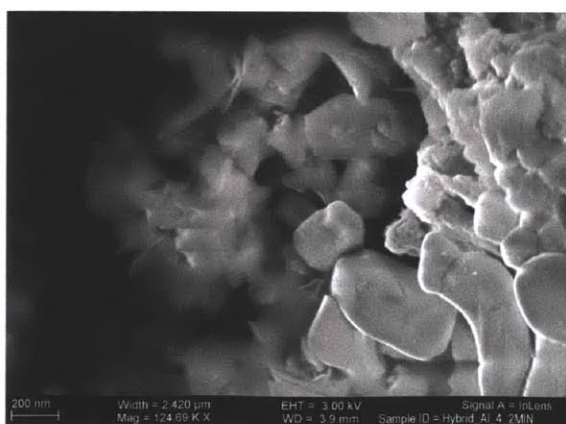
(c)



(d)



(e)



(f)

Figure A.1: High levels of silane deposited onto aluminum surfaces. (a) HCl 12 min etch at 31.7kx, (b) HCl 12 min etch at 5.95kx, (c) HCl 16 min etch at 860x, (d) HCl 16 min etch 18.47kx, (e) NaOH 15 min oxidation 32.61kx, (f) hybrid 4 min HCl etch, 20 min NaOH oxidation at 124.69kx magnifications.

Bibliography

- [1] J.B. Boreyko and C.H. Chen. Self-propelled dropwise condensate on superhydrophobic surfaces. *Physical review letters*, 103(18):184501, 2009.
- [2] RC Furneaux, WR Rigby, AP Davidson, et al. The formation of controlled-porosity membranes from anodically oxidized aluminium. *Nature*, 337(6203):147–149, 1989.
- [3] E.N. Wang N. Miljkovic, R. Enright. Effect of droplet morphology on growth dynamics and heat transfer during condensation on superhydrophobic nanostructured surfaces. *ACS Nano*, 6(2):1776–1785, 2012.
- [4] N. Miljkovic Y. Nam E.N. Wang R. Enright, N. Dou. Condensation on superhydrophobic copper oxide nanostructures. In *Proceedings of the 3rd Micro/Nanoscale Heat and Mass Transfer International Conference*, 2012.
- [5] JW Rose. Dropwise condensation theory and experiment: a review. *Proceedings of the Institution of Mechanical Engineers, Part A: Journal of Power and Energy*, 216(2):115–128, 2002.
- [6] N. Saleema, M. Farzaneh, RW Paynter, and DK Sarkar. Prevention of ice accretion on aluminum surfaces by enhancing their hydrophobic properties. *Journal of Adhesion Science and Technology*, 25, 1(3):27–40, 2011.
- [7] N. Saleema, DK Sarkar, RW Paynter, and X.G. Chen. Superhydrophobic aluminum alloy surfaces by a novel one-step process. *ACS Applied Materials & Interfaces*, 2010.
- [8] EM Sparrow and SH Lin. Condensation heat transfer in the presence of a noncondensable gas. *Journal of Heat Transfer*, 86:430, 1964.
- [9] John R. Thome. Engineering data book iii. Wolverine Tube, Inc., Lausanne, Switzerland, 2010.
- [10] John H. Lienhard V and John H. Lienhard IV. *A Heat Transfer Textbook*. Phlogiston Press, Cambridge, Massachusetts, fourth edition, 22 January 2011.
- [11] Y. Yin, T. Liu, S. Chen, T. Liu, and S. Cheng. Structure stability and corrosion inhibition of super-hydrophobic film on aluminum in seawater. *Applied Surface Science*, 255(5):2978–2984, 2008.
- [12] Z. Yu, Y. Yu, Y. Li, S. Song, S. Huo, and X. Han. Preparation and characterization of superhydrophobic surfaces on aluminum and stainless steel substrates. *Surface Review and Letters*, 17(3):375, 2010.